Tunable in-plane bihyperbolicity in bismuth monolayer

Xikui Ma,[*] Shuting Hou,[*] Mingzheng Wang, Yueheng Du, Chao Ding, Han Gao, Lei Sun, and Mingwen Zhao[†]
School of Physics, Shandong University, Jinan 250100, China

(Received 11 January 2024; revised 19 March 2024; accepted 16 April 2024; published 2 May 2024)

The distinctive hyperbolic properties of natural two-dimensional (2D) materials have garnered considerable attention in recent years due to their potential to surpass the limitations of metahyperbolic surfaces. It is essential to control hyperbolic regions and the sign of optical conductivities. This study introduces the concept of "bihyperbolicity" and establishes a critical connection between the semiconducting characteristics of 2D materials and their hyperbolic attributes. Through first-principles calculations, we illustrate the applicability of this strategy to materials such as the recently synthesized bismuth monolayer. The computations revealed that altering the type (*n* type or *p* type) of semiconducting bismuth monolayers can lead to a reversal of conductivity signs along two orthogonal directions, consequently enabling the precise regulation of hyperbolicity. The intriguing interplay between hyperbolicity and semiconductivity lays the foundation for crafting in-plane hyperbolic heterostructures using well-established semiconductor technologies. These heterostructures unlock a plethora of exotic optical phenomena, including negative refraction and negative reflection, thereby opening new horizons in optical engineering and device design.

DOI: 10.1103/PhysRevB.109.195401

I. INTRODUCTION

Surface-plasmon polaritons (SPPs), emerging from the collective oscillations of electrons coupled to photons at the material surface, exhibit fascinating characteristics, particularly their ability to generate highly confined electromagnetic fields. In particular, hyperbolic metasurfaces, strategically engineered to demonstrate opposing optical conductivity (or permittivity) along two distinct crystallographic directions, can facilitate the support of SPPs with exceptional confinement. This enables subwavelength waveguiding and substantially amplifies light-matter interactions at the nanoscale [1–6]. This unique property bears profound implications for a diverse array of applications, including sensing, nonlinear optics, and integrated photonic circuits [7–9].

Lately, there has been a growing fascination with natural van der Waals materials, which have proven to be a formidable tool for controlling electromagnetic waves [10–16]. Demonstrations of planar reflection, refraction, and focusing have been achieved by employing composite systems that include graphene, hexagonal boron nitride, and phase-changing materials [17–22], paying a way for polaritonics and on-chip integrated circuits. The emergence of two-dimensional (2D) materials has paved an exciting path for accommodating SPPs due to their unique plasmonic properties, encompassing a low damping rate, strong confinement, and exceptional tenability [13–16]. Natural hyperbolic 2D materials offer distinct advantages over metasurfaces. Their atomic-scale periodicity facilitates the generation of substantial wave vectors and eliminates the need for intricate surface patterning. Natural 2D hyperbolic materials demonstrate opposite signs in the imaginary components of conductivities along two orthogonal directions (x and y directions), i.e., $\mathrm{Im}\sigma_{xx} \times \mathrm{Im}\sigma_{yy} < 0$, within a specific frequency region known as the hyperbolic region. Within the hyperbolic region, the presence of two conductivities of opposite signs leads to hyperbolic isofrequency contours of SPPs, which facilitate significant propagation wave vectors, high photonic density of states, and directed SPP propagation [23–25].

The growing interest in harnessing 2D materials with inherent anisotropic electronic properties as natural platforms for hosting hyperbolic SPPs is driven by their advantages, including low loss and tunability. Several 2D materials, such as black phosphorus [26], α-MoO_3 [27–30], and WTe_2 [31,32] have been identified as capable of hosting anisotropic 2D plasmons. The dependence of plasmonic characteristics on the carrier density of these 2D materials enables remarkable tunability of the hyperbolic regions within these natural 2D hyperbolic materials [33–40]. Moreover, the emergence of moiré systems offers an efficient approach to tuning hyperbolicity by rotating two hyperbolic slabs with respect to one another [41–45]. Nevertheless, the precise manipulation of hyperbolicity, especially the signs of conductivities within a 2D hyperbolic material, remains an unattained goal. Furthermore, achieving the integration of distinct hyperbolicity within a single 2D material, which is anticipated to lead to a plethora of exotic optical phenomena, remains an unprecedented accomplishment in this field.

In this study, we have established a crucial connection between the semiconducting properties of 2D materials and their hyperbolic characteristics. We introduced a concept of bihyperbolicity to characterize the switchability between two distinct hyperbolic behaviors. By elucidating the correlations between semiconducting features and hyperbolic

[*]These authors contributed equally to this work.
[†]Corresponding author: zmw@sdu.edu.cn (M. Zhao)

properties, we have demonstrated the attainability of this concept in the recently synthesized bismuth monolayer. Our findings reveal that altering the type (n type or p type) of semiconducting bismuth monolayers can lead to a reversal of conductivity signs along two orthogonal directions, consequently enabling the regulation of hyperbolicity. This intriguing relationship between hyperbolicity and semiconductivity presents exciting possibilities for constructing in-plane hyperbolic heterostructures using well-established semiconductor technologies. Within these heterostructures, a wealth of exotic optical phenomena, including negative refraction and negative reflection, become attainable. This offers new perspectives in optical engineering and device design, opening avenues for innovative applications in the field.

II. THEORETICAL METHOD

A. First-principles calculations

We performed first-principles calculations utilizing density functional theory (DFT), employing the Vienna *ab initio* simulation package (VASP) [46]. This code adopted the projected augmented-wave method to model interactions between electrons and ions [47]. The exchange-correlation functional was self-consistently treated within the generalized gradient approximation, employing the Perdew-Burke-Ernzerhof (PBE) functional [48]. We set the cutoff energy to 500 eV. We conducted the structure relaxation and electronic properties of the bismuth monolayer using the k-point mesh of $25 \times 25 \times 1$. To prevent interactions between adjacent images, we included a vacuum space of 25 Å in the z direction. We performed full relaxation of lattice constants until atomic forces reached a threshold below 0.01 eV/Å and the total energy change was less than 10^{-5} eV. The spin-orbit coupling effect was included in these calculations. In our DFT calculations, we simulated the n-type or p-type characteristics of a semiconducting bismuth monolayer by either introducing additional electrons or removing electrons from the pristine bismuth monolayer. To preserve the electric neutrality of the entire system, compensatory background charges were added during our simulations.

For the construction of the bismuth monolayer's band structures, we utilized maximally localized Wannier functions, which were generated using the WANNIER90 package [49]. This strategy enabled us to obtain energy eigenvalues and eigenstates for subsequent polarization function calculations.

B. Linear response theory for plasmons

The dynamic dielectric function $\varepsilon(\mathbf{q}, \omega)$ was determined from the polarization function using the equation [50,51]

$$\varepsilon(\mathbf{q}, \omega) = 1 - V_{2\mathrm{D}}\Pi(\mathbf{q}, \omega), \tag{1}$$

where $V_{2\mathrm{D}} = 2\pi e^2/\varepsilon_r q$ is the Fourier transform of the Coulomb potential of 2D systems. The polarization function, $\Pi(\mathbf{q}, \omega)$, of a 2D system was calculated within the framework of the random phase approximation [52,53],

$$\Pi(\boldsymbol{q}, \omega) = \frac{g_s}{(2\pi)^2}\sum_{l,l'}\int d\boldsymbol{k}\frac{f(E_{\boldsymbol{k},l}) - f(E_{\boldsymbol{k}+\boldsymbol{q},l'})}{\omega + E_{\boldsymbol{k},l} - E_{\boldsymbol{k}+\boldsymbol{q},l'} + i\eta}F_{l,l'}(\boldsymbol{k}, \boldsymbol{q}), \tag{2}$$

with $F_{l,l'}(\boldsymbol{k}, \boldsymbol{q}) \equiv \langle \mathbf{k}, l|e^{-i\mathbf{q}\cdot\mathbf{r}}|\mathbf{k}+\mathbf{q}, l'\rangle\langle \mathbf{k}+\mathbf{q}, l'|e^{i\mathbf{q}\cdot\mathbf{r}}|\mathbf{k}, l\rangle$, where $g_s = 2$ is the spin degeneracy (we set $\hbar = 1$ and $e = 1$ hereafter), $E_{\mathbf{k}l}$ and $|\mathbf{k}, l\rangle$ represent the eigenvalues and eigenstates, respectively, with l denoting the band indices, which were obtained from first-principles calculations. We adopted a broadening parameter η of 0.05 eV. The Fermi-Dirac distribution function $f(E)$ acts as a step function at $T = 0$. Notably, the maximum wave vector of plasmons in bismuth monolayer considered in this work, 0.02 Å^{-1}, is far from the boundaries of the Brillouin zone, ~0.7 Å^{-1}. The local field effect arising from the inhomogeneous response can therefore be omitted in our calculations.

The electron energy loss spectrum (EELS) was calculated from the inverse of $\varepsilon(\mathbf{q}, \omega)$ using the expression

$$L(\mathbf{q}, \omega) = -\mathrm{Im}[1/\varepsilon(\mathbf{q}, \omega)]. \tag{3}$$

The plasmons are indicated by the peaks or local maxima of the EELS.

The optical conductivity $\sigma_{jj}(\omega)$ $(j = x, y)$ of bismuth monolayer was calculated using the expression

$$\begin{aligned}\sigma_{jj}(\omega) = {} & \frac{i}{(\omega + i\eta)}\sum_{\boldsymbol{k},l}\left(\partial E_{\boldsymbol{k},l}/\partial k_j\right)^2(-\partial f/\partial E_{\boldsymbol{k},l}) \\ & + i\sum_{\boldsymbol{k},l\neq l'}\frac{f(E_{\boldsymbol{k},l'}) - f(E_{\boldsymbol{k},l})}{(E_{\boldsymbol{k},l'} - E_{\boldsymbol{k},l}) - (\omega + i\eta)}\frac{1}{E_{\boldsymbol{k},l'} - E_{\boldsymbol{k},l}} \\ & \times |\langle \boldsymbol{k}, l|\hat{\upsilon}_j|\boldsymbol{k}, l'\rangle|^2,\end{aligned} \tag{4}$$

where the two terms denote the contributions stemming from intraband and interband transitions, as described by the Drude model [54] and the Kubo formalism [55], respectively. $\hat{\upsilon}_j = \partial/\partial k_j$ is the velocity operator.

III. RESULTS AND DISCUSSION

A. Bihyperbolicity model

We start from the intrinsic plasmons in anisotropic 2D materials without the presence of external electromagnetic waves. In the long-wavelength limit, with the damping rate excluded ($\eta = 0$), the polarization function expressed in Eq. (2) simplifies to an expression

$$\Pi(\boldsymbol{q}, \omega) = \left(\frac{D}{\omega^2} + \frac{S}{\omega^2 - \omega_b^2}\right)\frac{q^2}{\pi}, \tag{5}$$

with the intraband (Drude) weight of $D(\theta) = \pi\rho(E_F)(\langle\upsilon_x^2\rangle\cos^2\theta + \langle\upsilon_y^2\rangle\sin^2\theta)$ and the interband weight of $S(\theta) \approx \frac{g_s}{4\pi}\int\xi(\boldsymbol{k}, \theta)d^2\boldsymbol{k}$, both of which depend on the angle (θ) between the wave vector $\boldsymbol{q}$ and the x axis [56]. We define the averaged square Fermi velocities (ASFVs) as $\langle\upsilon_j^2\rangle = \sum_l\int\upsilon_j^2\delta(E_{\boldsymbol{k},l} - E_F)d\boldsymbol{k}/\sum_l\int\delta(E_{\boldsymbol{k},l} - E_F)d^2\boldsymbol{k}$ to characterize the anisotropy of the Fermi curves [57]. $\upsilon_j = \partial E_{\boldsymbol{k},l}/\partial k_j$ represents the electron velocity along the j

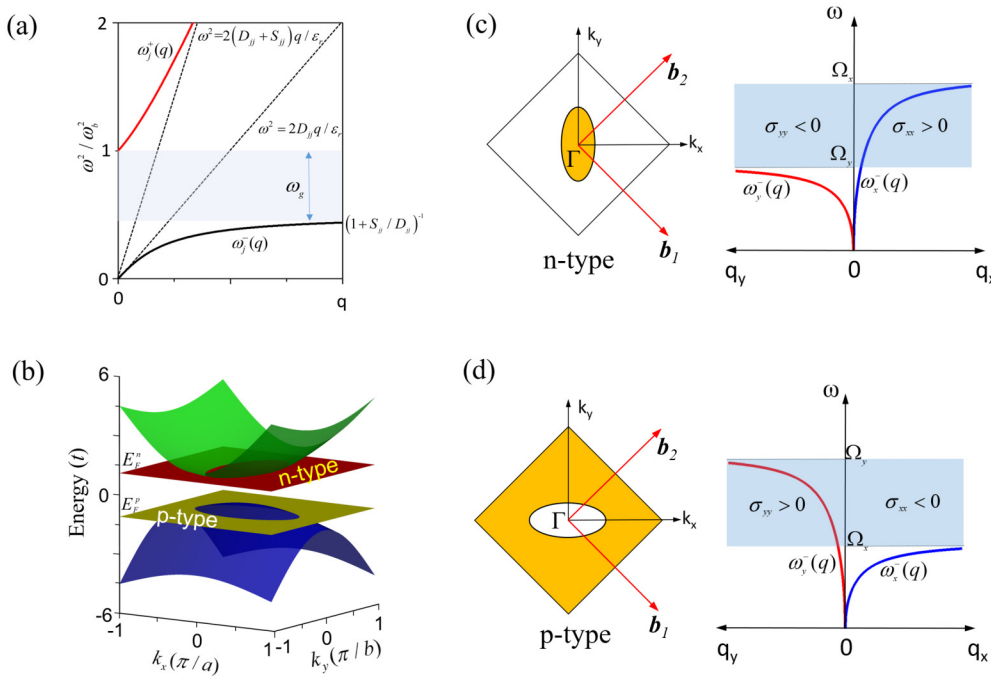

FIG. 1. Schematic representation of bihyperbolicity in 2D materials. (a) Plasmon dispersions in 2D materials given by Eq. (5). The two dashed lines represent the asymptotes of the two dispersions. (b) Schematic electronic band profiles of bihyperbolic 2D materials. E_F^n and E_F^p indicate the positions of Fermi levels for the *n*-type and *p*-type cases, respectively. (c) and (d) The correlation between the anisotropic Fermi surface (left panel) and the plasmon dispersions (right panel) for the *n*-type and *p*-type doping cases. The basis vectors of the reciprocal lattice are indicated by $\boldsymbol{b}_1$ and $\boldsymbol{b}_2$. The Brillouin zone is represented by the square. The yellow areas in the diagram indicate regions of electron occupation in the Brillouin zone.

direction. $\rho(E_F) = \frac{g_s}{(2\pi)^2}\sum_l \int \delta(E_{\boldsymbol{k},l} - E_F) d^2\boldsymbol{k}$ denotes the electron density of states at the Fermi level E_F.

The zeros of the dynamical dielectric function,$\varepsilon(\boldsymbol{q},\omega) = 0$, yield the following dispersion relation of plasmons:

$$\omega^{\pm}(\boldsymbol{q}) = \sqrt{\left(\kappa \pm \sqrt{\kappa^2 - 2\varepsilon_r D\omega_b^2 q}\right)/\varepsilon_r}, \tag{6}$$

with $\kappa = \omega_b^2\varepsilon_r/2 + q(D+S)$ and $+/-$ denoting the high-frequency/low-frequency branches, respectively. In the long-wavelength limit ($q \to 0$), Eq. (6) simplifies to $\omega^-(q \to 0) \approx (2Dq/\varepsilon_r)^{1/2}$ and $\omega^+(q \to 0) \approx \omega_b$, demonstrating the intraband and interband transition features, respectively. The $\omega \propto q^{1/2}$ dispersion relation for intraband plasmons has been reported in previous literatures [58,59]. For $q \gg \omega_b^2\varepsilon_r/2(D+S)$, the low-frequency branch attains its maximal value, $\omega_{\max}^- = \omega_b/\sqrt{1+S/D}$, while the high-frequency branch simplifies to $\omega^+(\boldsymbol{q}) \approx [2(D+S)q/\varepsilon_r]^{1/2}$, as illustrated in Fig. 1(a).

Notably, the anisotropy of plasmons is demonstrated by the dependence of both the intraband weight (D) and the interband weight (S) on the direction of wave vector $\boldsymbol{q}$. The relationship between the intraband weight (D) and the ASFV ($\langle \upsilon_j^2 \rangle$) enables us to analyze the anisotropy of plasmons based on the distribution of electron velocity along the Fermi contours. For instance, in the case of an elliptic Fermi contour, the electron velocity that aligns with the normal direction of the contour, causes the ASFV to be greater along the minor axis compared to the transverse direction. The degree of asymmetry between the x and y directions within the Fermi contour directly influences the anisotropy of the intrinsic plasmon dispersion relation, offering a valuable approach for predicting anisotropic plasmons within a 2D material.

The relation between conductivity $\sigma(\boldsymbol{q},\omega)$ and the polarization function in the homogeneous and local response limit, $\sigma(q,\omega) = ie^2\Pi(q,\omega)/q^2$ [50], leads to the expression of the conductivities along the x and y directions σ_{jj} as (setting $e = 1$)

$$\sigma_{jj}(\omega) = \frac{i}{\pi}\left(\frac{D_{jj}}{\omega} + \frac{S_{jj}}{\omega^2 - \omega_b^2}\right), \quad j = x, y, \tag{7}$$

where $D_{xx} = D(\theta = 0)$, $D_{yy} = D(\theta = \pi/2)$, $S_{xx} = S(\theta = 0)$, $S_{yy} = S(\theta = \pi/2)$. This expression corresponds to that of Ref. [12] without considering the damping rates ($\Gamma = \eta = 0$). The hyperbolic region can be precisely located by identifying the zero point (Ω_j) of Eq. (7) with

$$\Omega_j = \frac{\omega_b}{\sqrt{1 + S_{jj}/D_{jj}}}. \tag{8}$$

Interestingly, the zero points of conductivities coincide with the upper limits of the low-frequency anisotropic plasmons $\omega_{\max}^-$, $\omega_{j,\max}^- = \Omega_j$, thereby illustrating the connection between plasmon anisotropy and the hyperbolic region. Specifically, a pronounced anisotropy in the plasmon dispersion characterized by S_{jj}/D_{jj} could result in an extensive hyperbolic regime. Furthermore, given $S_{xx} = S_{yy}$, when $\langle \upsilon_x^2 \rangle > \langle \upsilon_y^2 \rangle$, we observe $\Omega_x > \Omega_y$ and consequently, $\sigma_{xx} > 0$ and $\sigma_{yy} < 0$ within the region of $\Omega_y \leqslant \omega \leqslant \Omega_x$, while conversely, $\sigma_{xx} < 0$ and $\sigma_{yy} > 0$ in the region of $\Omega_x \leqslant \omega \leqslant \Omega_y$ emerges. Previous research on controlling hyperbolic

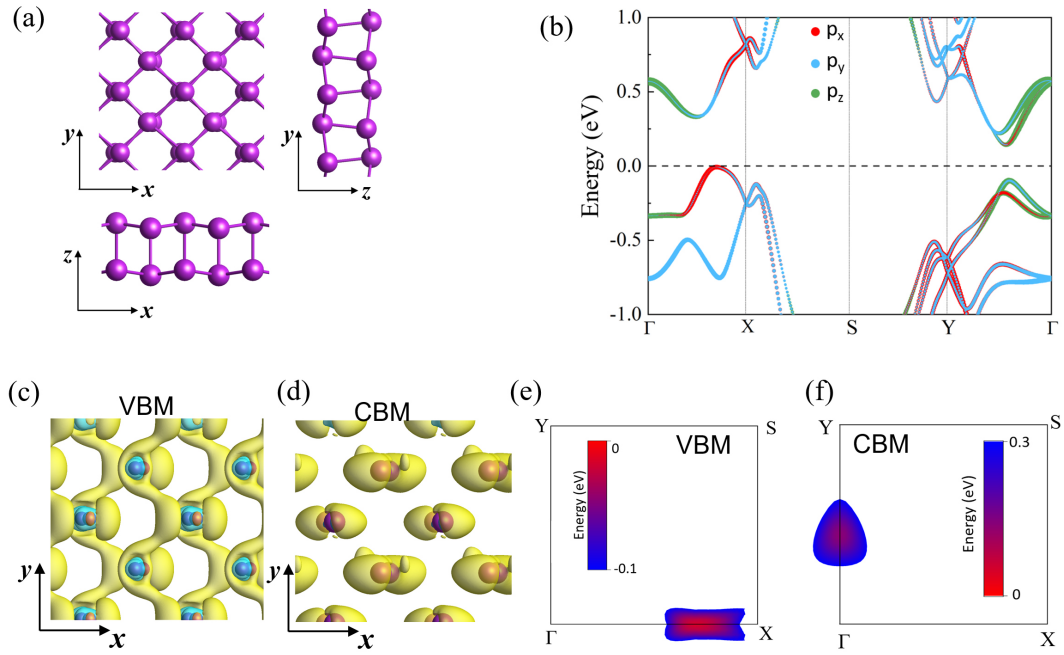

FIG. 2. Atomic configuration and electronic structure of bismuth monolayer. (a) Atomic configuration of bismuth monolayer consisting of two buckled rectangular sublayers. (b) Orbital-resolved electronic band structures of bismuth monolayer. The energy of the VBM indicated by the dashed line was set to zero. (c), (d) The isovalue profiles of the Kohn-Sham electron wave functions at the VBM and CBM, respectively. (e), (f) The anisotropic energy contours of electronic states near the VBM and CBM within the 1/4 Brillouin zone, respectively.

behavior has primarily concentrated on adjusting the extent of the hyperbolic region rather than transitioning between hyperbolic categories [33–40]. The intimate connection between D_{jj} and the electronic band structure in the vicinity of the Fermi level offers a powerful means to engineer the hyperbolicity of 2D materials. Specifically, if the valence and conduction bands of a semiconductor near the Fermi level exhibit opposite anisotropy along two orthogonal directions characterized by the different order of $\langle v_x^2 \rangle$ and $\langle v_y^2 \rangle$, one can potentially manipulate the signs of conductivities using well-established semiconductor doping processes. We refer to this unique characteristic as "bihyperbolicity."

We can illustrate this concept in a typical electronic band structure with the conduction band and the valence band exhibiting distinct anisotropy, represented by the elliptical isoenergy contours orientated along two orthogonal directions, as depicted in Fig. 1(b). The feasibility of this band structure is demonstrated using a tight-binding model [56]. For the collective oscillation of electrons in the conduction band (corresponding to the *n*-type scenario), the elliptical Fermi contour gives rise to a hyperbolic region with $\sigma_{xx} > 0$ and $\sigma_{yy} < 0$, because of $\langle v_x^2 \rangle > \langle v_y^2 \rangle$ and $D_{xx} > D_{yy}$, as shown in Fig. 1(c). Conversely, for the *p*-type case, the elliptical Fermi contour leads to $\langle v_x^2 \rangle < \langle v_y^2 \rangle$ and $D_{xx} < D_{yy}$, constructing a hyperbolic regime with $\sigma_{xx} < 0$ and $\sigma_{yy} > 0$, as depicted in Fig. 1(d). Therefore, by manipulating the position of the Fermi level, it becomes possible to switch between these two distinct hyperbolicities.

Bihyperbolicity in semiconductors represents the distinct anisotropic response of electrons and holes to an electric field, wherein they exhibit preferential movement respectively along two orthogonal directions. This distinctive feature presents a robust strategy for electrically modulating the propagation behaviors of SPPs via changing the carrier type, for instance, through gating techniques. Furthermore, it facilitates the creation of an in-plane heterostructure of two distinct hyperbolic regions, using well-established semiconductor doping processes. The development of such an in-plane hyperbolic heterostructure would result in exotic phenomena such as negative reflection and negative refraction [36], introducing innovative principles for advancement in the realms of subwavelength imaging, superlensing, quantum optics, and more.

B. Bihyperbolicity in bismuth monolayer

We examined the concept of bihyperbolicity in bismuth monolayer, which has been synthesized in recent experiments [60]. The bismuth monolayer consists of two buckled atomic sublayers featured by a rectangular unit cell, as depicted in Fig. 2(a). Each unit cell contains four Bi atoms with the lattice constants of $a = 4.79$ Å and $b = 4.51$ Å. The orbital-resolved electronic band structure calculated at the DFT + PBE level is presented in Fig. 2(b), which displays features of an indirect-bandgap semiconductor. Despite that the valence band maximum (VBM) and conduction band minimum (CBM) reside at different sites in the reciprocal space, they originate from distinct atomic orbitals. The electronic states near the VBM arise mainly from the p_x and p_y orbitals, whereas the states near the CBM come from the p_x and p_z orbitals. The anisotropic characteristics of the electronic states can be visualized from the corresponding Kohn-Sham electron wave-function profiles with remarkable spatial distribution difference along the x and y directions, as shown in Figs. 2(c) and 2(d). For instance, the wave function of the VBM displays a channel along the y direction, whereas the

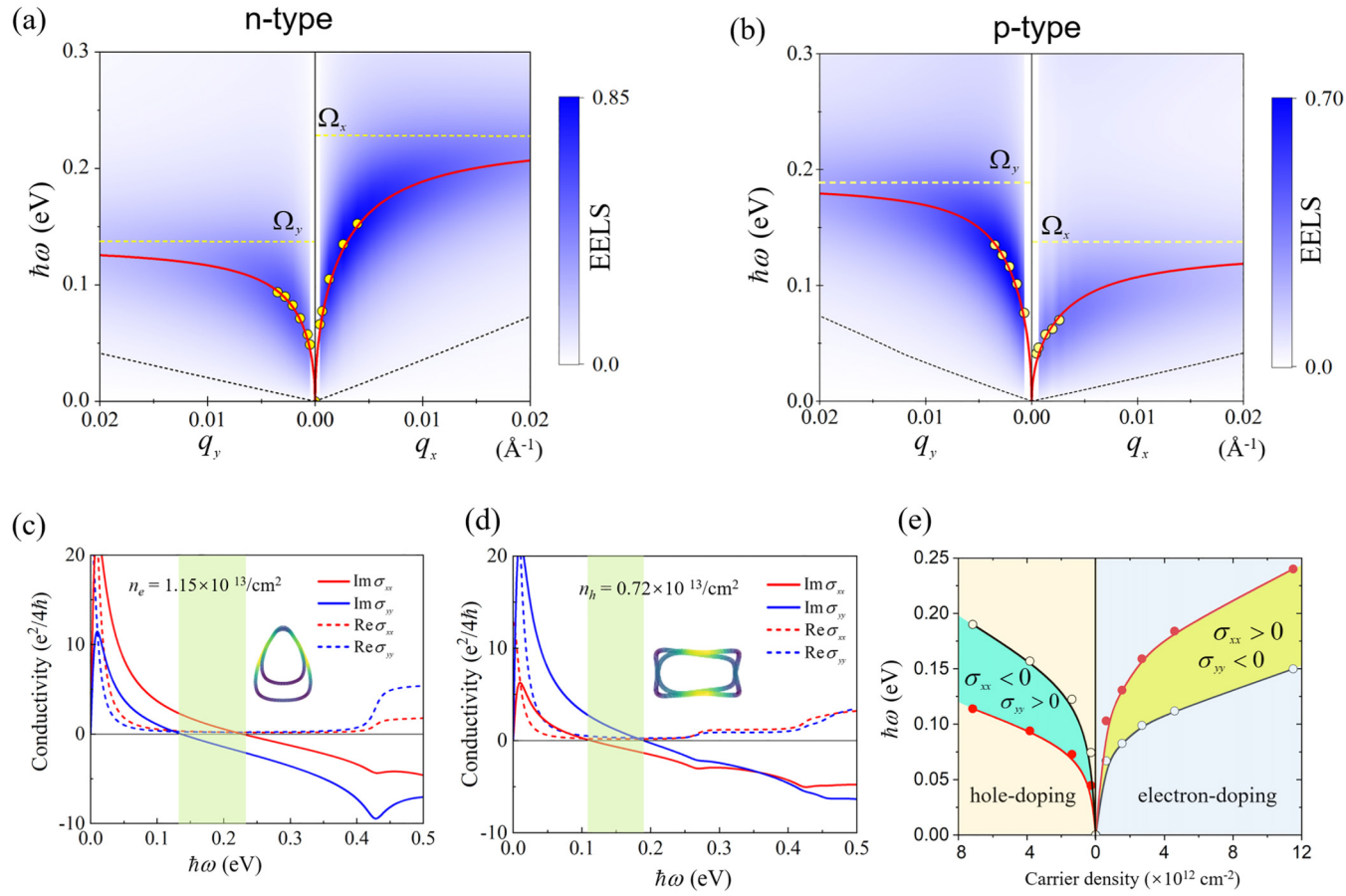

FIG. 3. The plasmonic properties and bihyperbolicity of bismuth monolayer. (a), (b) The electron energy loss spectra (EELS) of *n*-type and *p*-type bismuth monolayers at the doping concentration of $n_e = 1.15 \times 10^{13}\,\mathrm{cm}^{-2}$ and $n_h = 0.72 \times 10^{13}\,\mathrm{cm}^{-2}$, respectively. The yellow dots denote the specific plasmon modes obtained from first-principles calculations. The red lines represent the results of fitting these data using Eq. (6). The black dashed lines depict the boundaries of the intraband single-particle excitation regions. (c), (d) The optical conductivity of electron-doped and hole-doped bismuth monolayers. The Fermi-surface contours of the two cases are presented as the insets of these figures. (e) The variation of the hyperbolic regions of the hole-doped (left panel) and electron-doped (right panel) bismuth monolayer at different doping levels.

wave function of the CBM favors electron transport along the x direction. The anisotropic electronic states near the VBM and CBM are more evident from the isoenergy contours shown in Figs. 2(e) and 2(f). The isoenergy profile near the VBM exhibits contour patterns resembling an "athletic track" that extends along the x direction, resulting in $\langle \upsilon_x^2 \rangle < \langle \upsilon_y^2 \rangle$. Meanwhile, the isoenergy profile near the CBM takes on an amygdaloidal shape, distinctly pointing towards the y direction, showcasing $\langle \upsilon_x^2 \rangle > \langle \upsilon_y^2 \rangle$. The anisotropic electronic states of the bismuth monolayer essentially meet the criteria for bihyperbolic materials proposed in this study.

We further calculated the EELS of the bismuth monolayer to validate the bihyperbolicity from first-principles calculations. Figure 3(a) depicts the EELS of the *n*-type bismuth monolayer with the doping concentration of $n_e = 1.15 \times 10^{13}\,\mathrm{cm}^{-2}$. It is evident that the plasmon dispersion along the x direction has a higher upper-limit frequency than that along the y direction, which are respectively $\omega^{-}_{x,\mathrm{max}} = 228$ meV and $\omega^{-}_{y,\mathrm{max}} = 136$ meV. This yields a hyperbolic regime of $136\,\mathrm{meV} < \omega < 228$ meV satisfying $\sigma_{xx} > 0$ and $\sigma_{yy} < 0$, as shown in Fig. 3(c). For the hole-doped bismuth monolayer with the doping concentration of $n_h = 0.72 \times 10^{13}\,\mathrm{cm}^{-2}$, we got $\omega^{-}_{x,\mathrm{max}} = 113$ meV and $\omega^{-}_{y,\mathrm{max}} = 189$ meV, as shown in Fig. 3(b). This generates a hyperbolic regime of $113\,\mathrm{meV} < \omega < 189\,\mathrm{meV}$ with $\sigma_{xx} > 0$ and $\sigma_{yy} < 0$, as depicted in Fig. 3(d). The yellow dots indicate the specific data of the plasmon modes obtained by first-principles calculations. Fitting these data using Eq. (6), we got the dispersion relations of the plasmons along the x and y directions as depicted by the red lines in these figures, which are consistent with the EELS given by first-principles calculations. The fitting parameters are listed in Table I. The Fermi contours of these two types of bismuth monolayers are also presented in the insets of these figures. The results of our first-principles calculations are consistent with those from our simple tight-binding model, demonstrating the plausibility of 2D bihyperbolic materials.

Furthermore, we assessed the bihyperbolic behavior of the bismuth monolayer across various doping concentrations. Figure 3(e) illustrates the hyperbolic regions with the bismuth monolayer at varying doping levels. What becomes strikingly evident from our research is the remarkable tunability of the hyperbolic regime within the bismuth monolayer through electron and hole doping. It is intriguing to note that not only can the type of hyperbolic regime be altered, but also the

TABLE I. Fitting parameters of the plasmon dispersions in doped bismuth monolayers using Eq. (6). The *n*-type and *p*-type bismuth monolayers have the doping concentration of $n_e = 1.15 \times 10^{13}\,\mathrm{cm}^{-2}$ and the hole-doped bismuth monolayer with a doping level of $n_h = 0.72 \times 10^{13}\,\mathrm{cm}^{-2}$, respectively. $\varepsilon_r = 1$ was adopted.

	ω_b (eV)	Ω_x (eV)	Ω_y (eV)	D_{xx} (eV^2 Å)	D_{yy} (eV^2 Å)	S_{xx} (eV^2 Å)	S_{yy} (eV^2 Å)
n type	0.430	0.228	0.136	4.82	2.42	12.32	21.78
p type	0.260	0.133	0.189	1.33	4.06	3.75	5.42

specific band within the regime can be precisely engineered through controlled charge doping. As the doping level increases, both the frequency and the width of the hyperbolic region expand for both the *p*- and *n*-type doping cases, offering a promising strategy to engineer the hyperbolicity of the bismuth monolayer. Significantly, the doping level examined in this study falls within the range attainable under experimental conditions for 2D materials such as black phosphorus [61,62]. Furthermore, the negligible magnitudes of the real part of conductivity (Reσ_{xx} and Reσ_{yy}) within the hyperbolic regimes, as depicted in Figs. 3(c) and 3(d), suggest minimal energy loss, greatly enhancing the propagation of SPPs.

C. SPPs in bismuth monolayer

Finally, we investigate the directional properties of SPPs on the bismuth monolayer, which emerges from the coupling between the intrinsic plasmons and the electromagnetic field of the incident light. We consider the eigenmodes confined within the bismuth monolayer ($x-y$ plane) featured by $e^{i(q_x x+q_y y)}e^{-pz}$ (for $z>0$) and $e^{i(q_x x+q_y y)}e^{pz}$ for ($z<0$). The dispersion relations of the SPPs can be written as [6,63]

$$\left(q_x^2-k_0^2\right)\sigma_{xx}+\left(q_y^2-k_0^2\right)\sigma_{yy}=2ip\omega(\varepsilon_0+\mu_0\sigma_{xx}\sigma_{yy}/4). \quad (9)$$

In this expression, ε_0, μ_0, and $k_0=\omega\sqrt{\varepsilon_0\mu_0}$ represent the permittivity, permeability, and wave number in vacuum, $p=\sqrt{q_x^2+q_y^2-k_0^2}$. For scenarios with low damping (Im$\sigma \gg$ Reσ), Eq. (9) reduces to

$$\left(\tilde{q}_x^2-1\right)+\zeta\left(\tilde{q}_y^2-1\right)=\kappa\left(\tilde{q}_x^2+\tilde{q}_y^2-1\right)^{1/2}, \quad (10)$$

with $\tilde{q}_x=q_x/k_0$, $\tilde{q}_y=q_y/k_0$. The values of ζ and κ are derived from the optical conductivities of bismuth monolayer:$\zeta=Im\sigma_{yy}/Im\sigma_{xx}$ and $\kappa=[2\varepsilon_0/(\mu_0 Im\sigma_{xx}\times Im\sigma_{yy})-1/2]Im\sigma_{yy}(\varepsilon_0/\mu_0)^{-1/2}$. For $\zeta<0$, Eq. (10) exhibits two asymptotic lines given by $q_x^2+\zeta q_y^2=0$ for $q_x\gg k_0$ and $q_y\gg k_0$. This observation implies that the direction of propagation for SPP beams, which is determined by the group velocity normal to the contour line, can be characterized by an angle of $\varphi=\pm\tan^{-1}|\zeta|^{1/2}$ relative to the x direction.

We adopted the electron-doped bismuth monolayer with a doping concentration of $n_e = 1.15 \times 10^{13}\,\mathrm{cm}^{-2}$ and the hole-doped bismuth monolayer with a doping level of $n_h = 0.72 \times 10^{13}\,\mathrm{cm}^{-2}$ as illustrative cases to explore the hyperbolicity of the SPPs. Specifically, we selected the frequencies of $\omega = 151$, 174, and 194 meV for the electron-doped bismuth monolayer and $\omega = 129$, 149, and 169 meV for the hole-doped bismuth monolayer within their respective hyperbolic regions. Subsequently, we constructed isofrequency contours using Eq. (10), incorporating the pertinent optical conductivities obtained from first-principles calculations. The unmistakable hyperbolicity and asymptotic characteristics of these isofrequency contours emerged vividly in the two distinct hyperbolic regions, as depicted in Figs. 4(a) and 4(b). This unequivocally showcased the bismuth monolayer's bihyperbolic nature. Furthermore, the tunable bihyperbolicity of the bismuth monolayer opens the door to engineering in-plane hyperbolic heterostructures by combining *n*-type and *p*-type semiconducting materials. This capability empowers the manipulation of surface-plasmon propagation patterns.

To demonstrate the exotic optical scenarios within the in-plane hyperbolic heterostructure of bismuth monolayer, we simulated the propagation of electromagnetic wave beams with a frequency of $\omega = 140$ meV on this heterostructure by solving Maxwell's equations using the finite-element method. We examined a 2D bismuth sheet comprising both *n*-type and *p*-type domains, separated by a straight boundary. Positioned in the middle of the $\sigma_{xx} > 0$ and $\sigma_{yy} < 0$ domain is a *y*-directionally polarized dipole, strategically placed to stimulate surface electromagnetic waves. The optical conductivities at this specific frequency, derived from first-principles calculations, were set as follows: in the *n*-type domain, $\sigma_{xx} = 0.0005 + 0.123i$ mS and $\sigma_{yy} = 0.0005 - 0.007i$ mS, while in the *p*-type domain, $\sigma_{xx} = 0.0005 - 0.03i$ mS and $\sigma_{yy} = 0.0005 + 0.088i$ mS. The effective thickness of the sheet was set to 0.5 nm.

Two distinct boundary configurations are considered. One aligns along the *y* direction, while the other has an angle of 37 ° with respect to the *x* direction, as depicted in Figs. 4(c) and 4(d). Within each domain, the energy of the SPPs is directed into four narrow beams, with angles of $\varphi = \pm 13.4^\circ$ in the domain ($\sigma_{xx} > 0$ and $\sigma_{yy} < 0$) and $\varphi = \pm 59.7^\circ$ in the domain ($\sigma_{xx} < 0$ and $\sigma_{yy} > 0$) relative to the *x* direction. These values are consistent with Eq. (9), effectively showcasing the directional propagation of hyperbolic SPPs on the sheet [6,34]. Intriguingly, we observe an in-plane negative refraction (NRR) scenario as the electromagnetic waves across the interface. Additionally, for the second type of interface, we discover a noteworthy in-plane negative reflection. The instances of both negative refraction and negative reflection (NRL) can be explained by examining the hyperbolic isofrequency contours of the *n*-type and *p*-type bismuth monolayer. The boundary conditions for electromagnetic waves at the interface between the *n*-type and *p*-type bismuth monolayers enforce the conservation of transverse wave vectors on either side of the boundary, which in turn dictates the wave vectors for the refraction and reflection waves. Notably, the propagation direction of these refraction and reflection waves

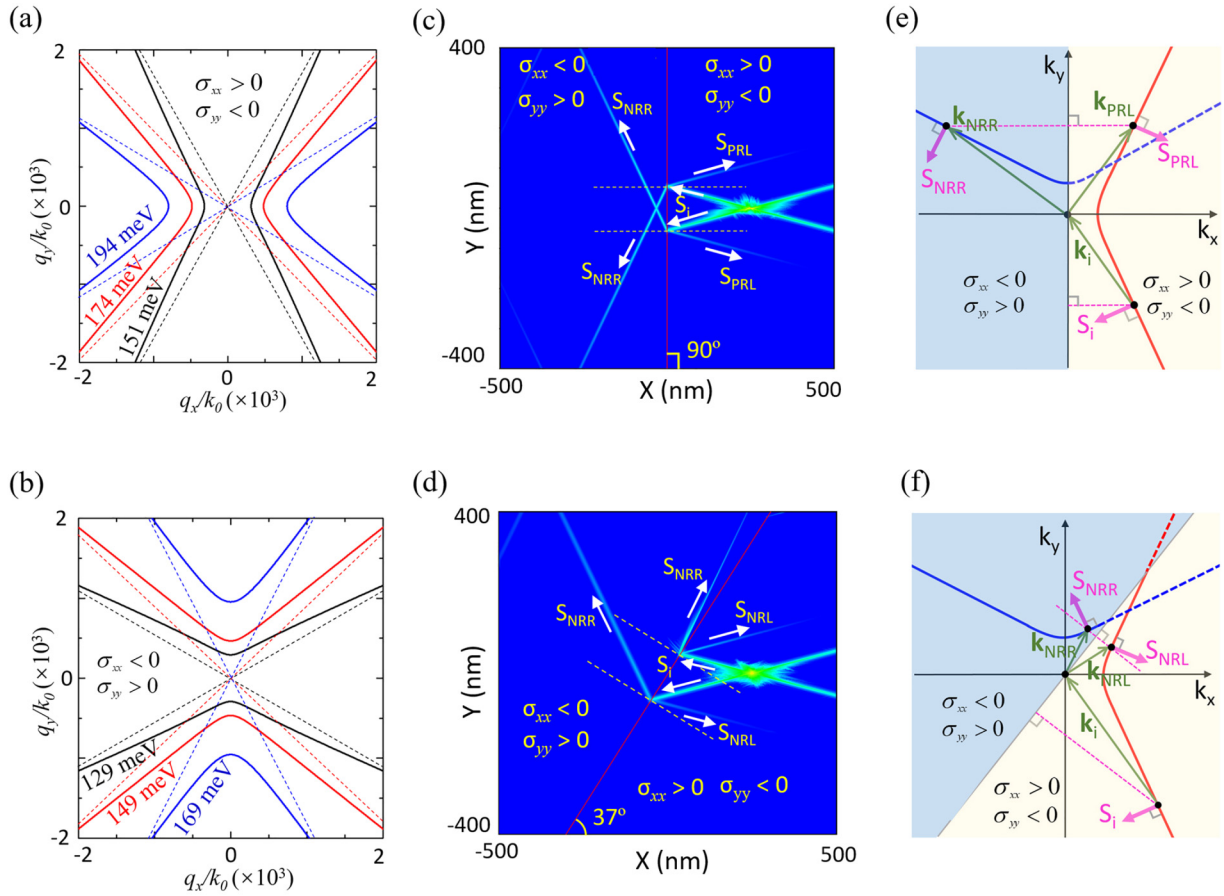

FIG. 4. The SPPs in bismuth monolayer. (a), (b) The isofrequency contours of bismuth monolayers at the doping concentration of $n_e = 1.15 \times 10^{13}\,\mathrm{cm}^{-2}$ and $n_h = 0.72 \times 10^{13}\,\mathrm{cm}^{-2}$, respectively. The dashed lines indicate the asymptotic lines. (c), (d) The spatial distribution of electric field $\boldsymbol{E}$ of the surface plasmons at $\omega = 140$ meV for the heterostructures with different interface configurations, respectively. The interface is marked by the red line. (e), (f) The corresponding isofrequency contours of the heterostructures. The Poynting vectors for the incident beam ($\mathbf{S_i}$), negative refraction ($\mathbf{S_{NRR}}$), negative reflection ($\mathbf{S_{NRL}}$), and positive reflection ($\mathbf{S_{PRL}}$) beams that are normal to the isofrequency contours are denoted.

is determined by the orientation of the Poynting vector, which is normal to the isofrequency contours.

It is important to note that a variety of 2D semiconducting materials exhibit intrinsic in-plane band anisotropy [64,65], beyond the bismuth monolayer. These materials include black phosphorus, ReX_2 (X = S, Se), MX (M = Sn, Ge; X = S, Se), MX_3 (M = Ti, Zr, Hf; X = S, Se), and YX (Y = Ge, Si; X = P, As), all of which possess reduced crystal symmetry. Some of these 2D materials have been demonstrated to display anisotropic optical properties [66]. However, to date, none has been identified as a bihyperbolic 2D material. Recent experimental breakthroughs have shown that optical conductivity in black phosphorus can be modulated by adjusting the charge density. This progress offers a promising approach to detect bihyperbolicity in bismuth monolayer.

IV. CONCLUSIONS

The investigation into bihyperbolicity in this study promises significant advancements, delving into the intricate interplay of material properties and revealing uncharted dimensions of semiconductivity within 2D materials. Particularly intriguing is the study's emphasis on bismuth monolayer, a material that has recently garnered significant attention. The computations presented in this research vividly showcase the distinct hyperbolic characteristics exhibited by n-type and p-type semiconducting bismuth monolayers. Notably, n-type semiconducting bismuth monolayers exhibit $\sigma_{xx} > 0$ and $\sigma_{yy} < 0$ hyperbolicity, while their p-type counterparts display the hyperbolicity of $\sigma_{xx} < 0$ and $\sigma_{yy} > 0$. This revelation ushers in a realm of exciting possibilities in the realm of 2D material engineering. Additionally, the recent experimental breakthrough in achieving anomalous optical phenomena, such as negative refraction and negative reflection, in natural hyperbolic materials [67–69], provides an exciting opportunity to explore the extraordinary properties of bismuth monolayers.

ACKNOWLEDGMENTS

This study is supported by the National Natural Science Foundation of China (Grant No. 12074218) and the Taishan Scholar Foundation of Shandong Province.

[1] W. L. Barnes, A. Dereux, and T. W. Ebbesen, Surface plasmon subwavelength optics, Nature (London) **424**, 824 (2003).

[2] J. B. Pendry, L. Martin-Moreno, and F. J. Garcia-Vidal, Mimicking surface plasmons with structured surfaces, Science **305**, 847 (2004).

[3] J. Lin, J. P. B. Mueller, Q. Wang, G. Yuan, N. Antoniou, X. Yuan, and F. Capasso, Polarization-controlled tunable directional coupling of surface plasmon polaritons, Science **340**, 331 (2013).

[4] A. A. High, D. C. Devlin, A. Dibos, M. Polking, D. S. Wild, J. Perczel, N. P. de Leon, M. D. Lukin, and H. Park, Visible-frequency hyperbolic metasurface, Nature (London) **522**, 192 (2015).

[5] J. S. Gomez-Diaz, M. Tymchenko, and A. Alu, Hyperbolic plasmons and topological transitions over uniaxial metasurfaces, Phys. Rev. Lett. **114**, 233901 (2015).

[6] A. Nemilentsau, T. Low, and G. Hanson, Anisotropic 2D materials for tunable hyperbolic plasmonics, Phys. Rev. Lett. **116**, 066804 (2016).

[7] D. Rodrigo, O. Limaj, D. Janner, D. Etezadi, F. J. G. de Abajo, V. Pruneri, and H. Altug, Mid-infrared plasmonic biosensing with graphene, Science **349**, 165 (2015).

[8] E. Ozbay, Plasmonics: Merging photonics and electronics at nanoscale dimensions, Science **311**, 189 (2006).

[9] S. Castilla, I. Vangelidis, V. V. Pusapati, J. Goldstein, M. Autore, T. Slipchenko, K. Rajendran, S. Kim, K. Watanabe, T. Taniguchi, L. Martín-Moreno, D. Englund, K. J. Tielrooij, R. Hillenbrand, E. Lidorikis, and F. H. L. Koppens, Plasmonic antenna coupling to hyperbolic phonon-polaritons for sensitive and fast mid-infrared photodetection with graphene, Nat. Commun. **11**, 4872 (2020).

[10] T. Low, A. Chaves, J. D. Caldwell, A. Kumar, N. Fang, P. Avouris, T. F. Heinz, F. Guinea, L. Martin-Moreno, and F. Koppens, Polaritons in layered two-dimensional materials, Nat. Mater. **16**, 182 (2017).

[11] W. Ma, P. Alonso-González, S. Li, A. Y. Nikitin, J. Yuan, J. Martín-Sánchez, J. Taboada-Gutiérrez, I. Amenabar, P. Li, S. Vélez, C. Tollan, Z. Dai, Y. Zhang, S. Sriram, K. Kalantar-Zadeh, S. T. Lee, R. Hillenbrand, and Q. Bao, In-plane anisotropic and ultra-low-loss polaritons in a natural van der Waals crystal, Nature (London) **562**, 557 (2018).

[12] D. N. Basov, M. M. Fogler, and F. J. García de Abajo, Polaritons in van der Waals materials, Science **354**, aag1992 (2016).

[13] L. Ju, B. Geng, J. Horng, C. Girit, M. Martin, Z. Hao, H. A. Bechtel, X. Liang, A. Zettl, Y. Shen, and F. Wang, Graphene plasmonics for tunable terahertz metamaterials, Nat. Nanotechnol. **6**, 630 (2011).

[14] A. N. Grigorenko, M. Polini, and K. S. Novoselov, Graphene plasmonics, Nat. Photon. **6**, 749 (2012).

[15] Z. Fei, A. S. Rodin, G. O. Andreev, W. Bao, A. S. McLeod, M. Wagner, L. Zhang, Z. Zhao, M. Thiemens, G. Dominguez, M. M. Fogler, A. H. Castro Neto, C. N. Lau, F. Keilmann, and D. N. Basov, Gate-tuning of graphene plasmons revealed by infrared nano-imaging, Nature (London) **487**, 82 (2012).

[16] J. N. Chen, M. Badioli, P. Alonso-González, S. Thongrattanasiri, F. Huth, J. Osmond, M. Spasenovic, A. Centeno, A. Pesquera, P. Godignon, A. Z. Elorza, N. Camara, F. J. G. de Abajo, R. Hillenbrand, and F. H. L. Koppens, Optical nano-imaging of gate-tunable graphene plasmons, Nature (London) **487**, 77 (2012).

[17] P. Alonso-González, A. Y. Nikitin, F. Golmar, A. Centeno, A. Pesquera, S. Vélez, J. Chen, G. Navickaite, F. Koppens, A. Zurutuza, F. Casanova, L. E. Hueso, and R. Hillenbrand, Controlling graphene plasmons with resonant metal antennas and spatial conductivity patterns, Science **344**, 1369 (2014).

[18] X. Lin, Y. Yang, N. Rivera, J. J. López, Y. Shen, I. Kaminer, H. Chen, B. Zhang, J. D. Joannopoulos, and M. Soljacic, All-angle negative refraction of highly squeezed plasmon and phonon polaritons in graphene−boron nitride heterostructures, Proc. Natl. Acad. Sci. USA **114**, 6717 (2017).

[19] T. G. Follan, A. Fali, S. T. White, J. R. Matson, S. Liu, N. A. Aghamiri, J. H. Edgar, R. F. Haglund, Y. Abate, and J. D. Caldwell, Reconfigurable infrared hyperbolic metasurfaces using phase change materials, Nat. Commun. **9**, 4371 (2018).

[20] K. Chaudhary, M. Tamagnone, X. Yin, C. M. Spägele, S. L. Oscurato, J. Li, C. Persch, R. Li, N. A. Rubin, L. A. Jauregui, K. Watanabe, T. Taniguchi, P. Kim, M. Wuttig, J. H. Edgar, A. Ambrosio, and F. Capasso, Polariton nanophotonics using phase-change materials, Nat. Commun. **10**, 4487 (2019).

[21] P. Li, X. Yang, T. W. Mass, J. Hanss, M. Lewin, A. K. U. Michel, M. Wuttig, and T. Taubner, Infrared hyperbolic metasurface based on nanostructured van der Waals materials, Nat. Mater. **15**, 870 (2016).

[22] N. A. Aghamiri, G. Hu, A. Fali, Z. Zhang, J. Li, S. Balendhran, S. Walia, S. Sriram, J. H. Edgar, S. Ramanathan, A. Alu, and Y. Abate, Reconfigurable hyperbolic polaritonics with correlated oxide metasurfaces, Nat. Commun. **13**, 4511 (2022).

[23] P. Li, I. Dolado, F. J. Alfaro-Mozaz, F. Casanova, L. E. Hueso, S. Liu, J. H. Edgar, A. Y. Nikitin, S. Vélez, and R. Hillenbrand, Infrared hyperbolic metasurface based on nanostructured van der Waals materials, Science **359**, 892 (2018).

[24] P. N. Li, G. Hu, I. Dolado, M. Tymchenko, C. Qiu, F. J. Alfaro-Mozaz, F. Casanova, L. E. Hueso, S. Liu, J. H. Edgar, S. Vélez, A. Alu, and R. Hillenbrand, Collective near-field coupling and nonlocal phenomena in infrared-phononic metasurfaces for nano-light canalization, Nat. Commun. **11**, 3663 (2020).

[25] Z. Zheng, N. Xu, S. L. Oscurato, M. Tamagnone, F. Sun, Y. Jiang, Y. Ke, J. Chen, W. Huang, W. L. Wilson, A. Ambrosio, S. Deng, and H. Chen, A mid-infrared biaxial hyperbolic van der Waals crystal, Sci. Adv. **5**, eaav8690 (2019).

[26] E. van Veen, A. Nemilentsau, A. Kumar, R. Roldán, M. I. Katsnelson, T. Low, and S. Yuan, Tuning two-dimensional hyperbolic plasmons in black phosphorus, Phys. Rev. Appl. **12**, 014011 (2019).

[27] F. L. Ruta, B. S. Y. Kim, Z. Sun, D. J. Rizzo, A. S. McLeod, A. Rajendran, S. Liu, A. J. Millis, J. C. Hone, and D. N. Basov, Surface plasmons induce topological transition in graphene/α-MoO_3 heterostructures, Nat. Commun. **13**, 3719 (2022).

[28] Y. Zeng, Q. Ou, L. Liu, C. Zheng, Z. Wang, Y. Gong, X. Liang, Y. Zhang, G. Hu, Z. Yang, C. Qiu, Q. Bao, H. Chen, and Z. Dai, Tailoring topological transitions of anisotropic polaritons by interface engineering in biaxial crystals, Nano Lett. **22**, 4260 (2022).

[29] H. Hu, N. Chen, H. Teng, R. Yu, Y. Qu, J. Sun, M. Xue, D. Hu, B. Wu, C. Li, J. Chen, M. Liu, Z. Sun, Y. Liu, P. Li, S. Fan, F. J. de Abajo, and Q. Dai, Doping-driven topological polaritons in graphene/α-MoO_3 heterostructures, Nat. Nanotechnol. **17**, 940 (2022).

[30] A. Bapat, S. Dixit, Y. Gupta, T. Low, and A. Kumar, Gate tunable light–matter interaction in natural biaxial hyperbolic van der Waals heterostructures, Nanophotonics **11**, 2329 (2022).

[31] Z. Torbatian, D. Novko, and R. Asgari, Tunable low-loss hyperbolic plasmon polaritons in a $T_d - WTe_2$ single layer, Phys. Rev. Appl. **14**, 044014 (2020).

[32] C. Wang, S. Huang, Q. Xing, Y. G. Xie, C. Song, F. Wang, and H. Yan, Van der Waals thin films of WTe_2 for natural hyperbolic plasmonic surfaces, Nat. Commun. **11**, 1158 (2020).

[33] H. Gao, C. Ding, L. Sun, X. Ma, and M. Zhao, Robust broadband directional plasmons in a $MoOCl_2$ monolayer, Phys. Rev. B **104**, 205424 (2021).

[34] S. Hou, M. Wang, H. Gao, C. Ding, X. Zhang, L. Sun, X. Ma, Y. Li, and M. Zhao, Broadband hyperbolic plasmons in aluminum disulfide monolayer and its analogues: The role of orbital anisotropy, Phys. Rev. B **107**, 195410 (2023).

[35] M. Wang, H. Gao, C. Ding, X. Zhang, S. Hou, L. Sun, X. Ma, Y. Li, and M. Zhao, Hyperbolic plasmons on natural biphenylene surface, Carbon **213**, 118307 (2023).

[36] T. Zhang, C. Zheng, Z. Chen, and C. Qiu, Negative reflection and negative refraction in biaxial van der Waals materials, Nano Lett. **22**, 5607 (2022).

[37] W. Geng, H. Gao, C. Ding, L. Sun, X. Ma, Y. Li, and M. Zhao, Highly-anisotropic plasmons in two-dimensional hyperbolic copper borides, Opt. Express **30**, 5596 (2022).

[38] M. Dehdast, Z. Valiollahi, M. Neek-Amal, B. Van Duppen, F. M. Peeters, and M. Pourfath, Tunable natural terahertz and mid-infrared hyperbolic plasmons in carbon phosphide, Carbon **178**, 625 (2021).

[39] G. Jia, J. Luo, H. Wang, Q. Ma, Q. Liu, H. Dai, and R. Asgari, Two-dimensional natural hyperbolic materials: From polaritons modulation to applications, Nanoscale **14**, 17096 (2022).

[40] M. Dehdast, M. Neek-Amal, C. Stampfl, and M. Pourfath, Strain engineering of hyperbolic plasmons in monolayer carbon phosphide: A first-principles study, Nanoscale **15**, 2234 (2023).

[41] O. V. Kotov and Y. E. Lozovik, Hyperbolic hybrid waves and optical topological transitions in few-layer anisotropic metasurfaces, Phys. Rev. B **100**, 165424 (2019).

[42] G. Hu, A. Krasnok, Y. Mazor, C. Qiu, and A. Alù, Moiré hyperbolic metasurfaces, Nano Lett. **20**, 3217 (2020).

[43] G. Hu, Q. Ou, G. Si, Y. Wu, J. Wu, Z. Dai, A. Krasnok, Y. Mazor, Q. Zhang, Q. Bao, C. Qiu, and A. Alù, Topological polaritons and photonic magic angles in twisted α-MoO_3 bilayers, Nature (London) **582**, 209 (2020).

[44] Z. Zheng, F. Sun, W. Huang, J. Jiang, R. Zhan, Y. Ke, H. Chen, and S. Deng, Phonon polaritons in twisted double-layers of hyperbolic van der Waals crystals, Nano Lett. **20**, 5301 (2020).

[45] J. H. Duan, N. Capote-Robayna, J. Taboada-Gutiérrez, G. Álvarez-Pérez, I. Prieto, J. Martín-Sánchez, A. Y. Nikitin, and P. Alonso-González, Twisted nano-optics: Manipulating light at the nanoscale with twisted phonon polaritonic slabs, Nano Lett. **20**, 5323 (2020).

[46] G. Kresse and J. Furthmüller, Efficient iterative schemes for *ab initio* total-energy calculations using a plane-wave basis set, Phys. Rev. B **54**, 11169 (1996).

[47] P. E. Blöchl, Projector augmented-wave method, Phys. Rev. B **50**, 17953 (1994).

[48] J. P. Perdew, K. Burke, and M. Ernzerhof, Ernzerhof, generalized gradient approximation made simple, Phys. Rev. Lett. **77**, 3865 (1996).

[49] A. A. Mostofi, J. R. Yates, Y. S. Lee, I. Souza, D. Vanderbilt, and N. Marzari, WANNIER90: A tool for obtaining maximally-localised Wannier functions, Comput. Phys. Commun. **178**, 685 (2008).

[50] P. A. D. Gonçalves and N. M. Peres, *An Introduction to Graphene Plasmonics* (World Scientific, Singapore, 2016).

[51] S. Das Sarma and E. H. Hwang, Collective modes of the massless Dirac plasma, Phys. Rev. Lett. **102**, 206412 (2009).

[52] S. L. Adler, Quantum theory of the dielectric constant in real solids, Phys. Rev. **126**, 413 (1962).

[53] N. Wiser, Dielectric constant with local field effects included, Phys. Rev. **129**, 62 (1963).

[54] L. A. Falkovsky and A. A. Varlamov, Space-time dispersion of graphene conductivity, Eur. Phys. J. B **56**, 281 (2007).

[55] V. P. Gusynin, S. G. Sharapov, and J. P. Carbotte, Unusual microwave response of Dirac quasiparticles in graphene, Phys. Rev. Lett. **96**, 256802 (2006).

[56] See Supplemental Material at http://link.aps.org/supplemental/10.1103/PhysRevB.109.195401 for the derivation of Eq. (5) and the tight-binding model of bihyperbolicity.

[57] H. Gao, X. Zhang, C. Ding, X. Ma, M. Wang, Y. Li, and M. Zhao, Highly directional and carrier density-independent plasmons in quasi-one-dimensional electron gas systems, Commun. Phys. **6**, 342 (2023).

[58] A. S. Rodin and A. H. Castro Neto, Collective modes in anisotropic double-layer systems, Phys. Rev. B **91**, 075422 (2015).

[59] T. Low, R. Roldán, H. Wang, F. Xia, P. Avouris, L. M. Moreno, and F. Guinea, Plasmons and screening in monolayer and multilayer black phosphorus, Phys. Rev. Lett. **113**, 106802 (2014).

[60] J. Gou, H. Bai, X. Zhang, Y. Huang, S. Duan, A. Ariando, S. Y. A. Yang, L. Chen, Y. Lu, and A. T. S. Wee, Two-dimensional ferroelectricity in a single-element bismuth monolayer, Nature (London) **617**, 67 (2023).

[61] M. Liu, S. Feng, Y. Hou, S. Zhao, L. Tang, J. Liu, F. Wang, and B. Liu, High yield growth and doping of black phosphorus with tunable electronic properties, Mater. Today **36**, 91 (2020).

[62] F. Xia, H. Wang, and Y. Jia, Rediscovering black phosphorus as an anisotropic layered material for optoelectronics and electronics, Nat. Commun. **5**, 4458 (2014).

[63] G. W. Hanson, Dyadic Green's functions for an anisotropic nonlocal model of biased grephene, IEEE Trans. Antennas Propag. **56**, 747 (2008).

[64] C. Wang, G. Zhang, S. Huang, Y. Xie, and H. Yan, The optical properties and plasmonics of anisotropic 2D materials, Adv. Opt. Mater. **8**, 1900996 (2020).

[65] L. Li, W. Han, L. Pi, P. Niu, J. Han, C. Wang, B. Su, H. Li, J. Xiong, Y. Bando, and T. Zhai, Emerging in-plane anisotrpoic two-dimensional materials, InfoMat. **1**, 54 (2019).

[66] S. Biswas, W. S. Whitney, M. Y. Grajower, K. Watanabe, T. Taniguchi, H. A. Bechtel, G. R. Rossman, and H. A. Atwater, Tunable intraband optical conductivity and polarization-dependent epsilon-near-zero behavior in black phosphours, Sci. Adv. **7**, eabd4623 (2021).

[67] H. Hu, N. Chen, H. Teng, R. Yu, M. Xue, K. Chen, Y. Xiao, Y. Qu, D. Hu, J. Chen, Z. Sun, P. Li, F. J. García de Abajo,

and Q. Dai, Gate-tunable negative refraction of mid-infrared polarization, Science **379**, 558 (2023).

[68] A. J. Sternbach, S. L. Moore, A. Rikhter, S. Zhang, R. Jing, Y. Shao, B. S. Y. Kim, S. Xu, S. Liu, J. H. Edgar, A. Rubio, C. Dean, J. Hone, M. M. Fogler, and D. N. Basov, Negative refraction in hyperbolic hetero-bicrystals, Science **379**, 555 (2023).

[69] G. Alvarez-Pérez, J. Duan, J. Taboada-Gutiérrez, Q. Ou, E. Nikulina, S. Liu, J. H. Edgar, Q. Bao, V. Giannini, R. Hillenbrand, J. Martín-Sánchez, A. Y. Nikitin, and P. Alonso-González, Negative reflection of nanoscale-confined polaritons in a low-loss natural medium, Sci. Adv. **8**, eabp8486 (2022).